# Shining a New Light on the Riddle of Shear

by Jack J. Poldon, Neil A. Hoult, and Evan C. Bentz

**D**espite over 100 years of reinforced concrete research, the precise load-carrying mechanism for shear is still up for debate.[1] Past researchers have characterized shear failures through empirical relations based on limited measurement data leading to design codes around the world using different approaches to estimate shear strength. But with the emergence of distributed sensors, namely distributed fiber optic sensors (DFOS) and digital image correlation (DIC), the potential now exists to characterize the behavior of reinforced concrete with a new level of accuracy, and to find an answer to the riddle of shear.[2]

While the ACI shear provisions for members with stirrups are well established, there are numerous cases where a more robust understanding is helpful, such as assessing the strength of existing structures designed by older codes or with poor details, and displacement-sensitive members subjected to high shear forces like transfer girders. The irregularly shaped and nonorthogonal transfer girders in Fig. 1, for example, require a robust understanding of shear to ensure proper performance at both serviceability and ultimate limit states (ULS). In cases where a transfer girder supports many stories of a building, the displacement of these highly loaded members can govern design. Also, as the industry moves toward reducing its carbon footprint, finding efficiencies in design will become increasingly important and this will only be successful if the limitations of the basic design models are understood.

This article examines the ACI 318 assumptions and design approaches for shear using the results from beam tests with varying shear reinforcement designs measured with emerging sensor technologies. After the research campaign is described, the distributed measurements are presented with discussion of the key insights. Finally, takeaway messages are presented for designers.

## Experimental Campaign

### Specimen design

This study focused on three reinforced concrete beams named JP-1, JP-2, and JP-3 which were designed with varying shear reinforcement, as summarized in Fig. 2 and tested in three-point bending. Specimen JP-1, which contained slightly more than the ACI minimum shear reinforcement, had a shear reinforcement ratio ($\rho_v = A_v / (b_w \cdot s)$) of 0.11% using single legged 10M stirrups at a spacing of 300 mm, and was designed to fail in shear before the longitudinal reinforcement yielded. Specimen JP-2 had a $\rho_v$ of 0.22% using double legged 10M stirrups at 300 mm spacing, and was designed to fail in shear at about the same applied load as that required to cause a flexural failure. Specimen JP-3 contained the most shear reinforcement. It had a $\rho_v$ of 0.33% using double legged 10M stirrups at a 200 mm spacing and was designed to reach its flexural strength and undergo extensive plastic deformation before a shear failure was expected to eventually occur.

Other than the levels of shear reinforcement, the three beams had the same overall geometry with a length of 4880 mm, height of 750 mm, and width of 300 mm. The beams also contained the same amount of tension reinforcement ($\rho = A_s / (b \cdot d) = 1.47\%$) provided by three 35M bars. Specimen JP-1 contained a single 20M bar for compression reinforcement, while JP-2 and JP-3 both contained two 20M bars for compression reinforcement. Uniaxial tension test results for the 10M and 35M are shown in Fig. 2, along with the Ramberg-Osgood coefficients used to translate the measured DFOS strain measurements to stresses.[3] The 20M steel had a measured yield strength of 430 MPa.



**Fig. 1: Transfer girders at the Paul S. Sarbanes Transit Center in Spring City, MD, USA** *(photo courtesy of Evan Bentz)*
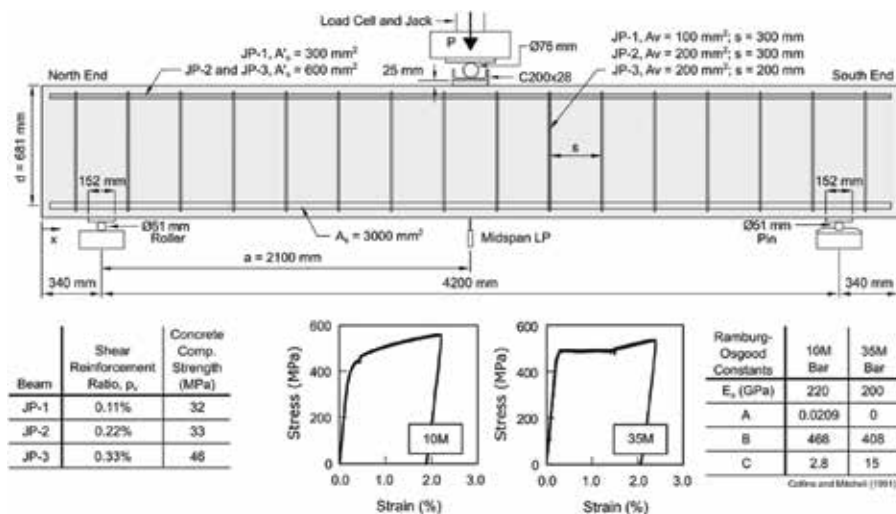
**Fig. 2: Test set-up, reinforcement for the three beam specimens, and material properties**



**Fig. 3: Reinforcement cage of specimen JP-2 being lowered into the forms prior to concrete casting with DFOS bonded to the 20M reinforcement and 10M stirrups visible**

The concrete mixture was intended to be the same for all three beams, supplied by a ready mixed concrete company, with a specified 28-day compressive strength of 35 MPa and a maximum coarse aggregate size of 19 mm. On the dates of beam testing, concrete cylinder tests determined the compressive strength of the concrete to be 32 MPa, 33 MPa, and 46 MPa, for JP-1, JP-2, and JP-3, respectively.

### Distributed sensors

The distributed fiber optic sensing technology employed in this study is based on the measurement of Rayleigh backscatter, which is well suited for studying reinforcement strains because of its ability to measure distributed strain accurately and over many meters of fiber. DFOS works by shining a laser down the core of a fiber optic cable, which is only 8 micrometers in diameter (smaller than a human hair), and measuring the light that reflects off internal flaws back to the instrument. Strain measurements can be taken with variable sensor gauge lengths and spacings, where measurement

accuracy of 1 microstrain within the optical fiber's core is possible.[4] In this study, 10 mm gauge lengths and sensor spacings were used. For the three beams, the fiber optic cables were bonded to the reinforcement cage prior to concrete casting[5] as shown in Fig. 3. Fiber optic cables were installed on both longitudinal ribs of the reinforcing bars so the effects of bar bending could be measured but also mitigated by averaging the measurements. Considering all the bonded fiber optic cables on the steel reinforcement and the 10 mm sensor spacing, the three beams collectively contained the equivalent of about 20,000 conventional strain gauges.

The DIC technique employed in this study was a two-dimensional (2-D) DIC algorithm known as geoPIV,[6] which operates by tracking the translation of subsets (a specific group of pixels) throughout a sequence of digital images. When the relative movement of subsets is determined, crack width and slip measurements can be found as shown by Hoult et al.[7]

### Testing protocol

As shown in Fig. 2, the beams were tested in three-point bending with an overall span on-center of 4200 mm. Thus, with an effective depth (*d*) of 681 mm, the shear span-to-depth (*a/d*) ratio was 3.1, meaning the specimens were slender beams from an analysis point of view. The beams were loaded in displacement control at a rate of 1 mm/min with a 2000 kN capacity hydraulic jack. Loading was paused every 50 kN for approximately 20 minutes so the DFOS and DIC measurements could be recorded. In addition to the distributed sensors, linear potentiometers (LPs) measured the beam displacements at midspan while the applied load was measured with a load cell as shown in Fig. 2.

## Measurements and Insights
### Shear and bending deflections

The load (*P*) versus midspan deflection responses ($\Delta_{Exp.}$ curves) of the three beams are summarized in Fig. 4(a) through (c), which shows that JP-1 and JP-2 experienced brittle shear failures, while JP-3 underwent flexural yielding before an anchorage failure was observed at the north end.[5] Because these $\Delta_{Exp.}$ measurements represent the total displacement from a displacement transducer placed at the midspan of the beams, $\Delta_{Exp.}$ includes both bending deformations from curvature and shear deflections from shear strains, though the latter are usually ignored by designers. Distributed sensing enables the bending and shear deflection components to be decoupled as they were measured independently.

The DFOS longitudinal reinforcement strains could be

used to calculate the bending deflections ($\Delta_{bending}$) while DIC could be used to calculate the shear deflections ($\Delta_{shear}$). The flexural deflections were determined through taking the DFOS strains along the top and bottom reinforcement bars, computing a curvature graph with length, and then performing double integration to find the deflected shape.[8] Meanwhile, distributed shear strains ($\gamma$) were calculated along the north shear spans of the three beams by placing the DIC subsets in a similar arrangement as can be done with two perpendicular displacement transducers installed at a 45-degree angle to the longitudinal axis of the beam.[9] The average shear strain along the north shear span was then multiplied by shear span ($a$) (where, $\Delta_{shear} = \gamma \cdot a$) to find the shear deflection for any given load stage.[8]

As seen in Fig. 4(a) through (c), the total beam deflections calculated from the distributed measurements ($\Delta_{total,ds}$) are in good visual agreement with those obtained directly from the linear potentiometers placed under the beams' midspan. Additionally, until an applied load of about 400 kN, the total beam deflections were primarily due to bending because the beams had not yet developed shear cracks. However, as significant diagonal cracks developed, the shear deflection ($\Delta_{shear}$) became non-negligible. This meant that at service conditions, the shear deflection represented about 25% of the total (where service conditions were taken as 60% of the ACI 318 estimated member strength), as seen in Fig. 4(d). The percentage of total deflection attributable to shear ($\Delta_{shear} / \Delta_{total,ds}$) was found to increase with applied loading, where at the ultimate load it represented up to 42% for specimen JP-1. The proportion of total deflection due to shear at the ultimate load went down as the shear reinforcement ratio increased partly because JP-3 did not fail in shear, but also because higher shear reinforcement levels result in lower shear strains for a given shear stress. It can be concluded from Fig. 4 that curvature plus shear strain is sufficient to model overall member displacement in a transfer girder, and many designs of such members are likely systematically underestimating displacements by ignoring shear strains.

## Components of shear-carrying mechanism

The real power of distributed sensing for understanding shear is not the ability to measure what a dial gauge could, but to help understand what is happening inside a member during loading. The ability to determine internal steel stresses and crack movement at any location in the member allows for the generation of detailed free body diagrams (FBDs) based on the fundamentals of equilibrium, compatibility, and stress-strain relationships. Figure 5 shows an FBD of beam JP-2 at an applied load of 735 kN cut along a shear crack that

formed in the north span, defined as crack JP-2 C2.

The steel forces displayed are not based on a numerical model or code equation but rather on direct strain measurements from the distributed sensors and material models.[10] In Fig. 5, the stirrup tension forces ($F_{t,S5}$ and $F_{t,S6}$) are based on the peak DFOS strains measured on the two legs of the double legged stirrups, which were transformed into stresses through the Ramberg-Osgood function presented in
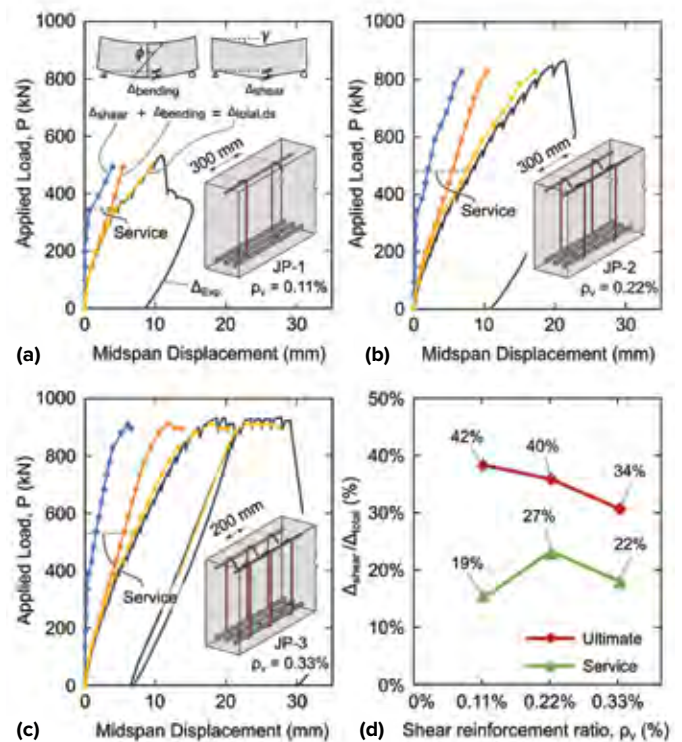
**Fig. 4: Load versus midspan deflection responses: (a) load-displacement of JP-1 with a depiction of shear and bending components; (b) JP-2; (c) JP-3; and (d) shear displacement as a percentage of total displacement at service and ultimate loads**
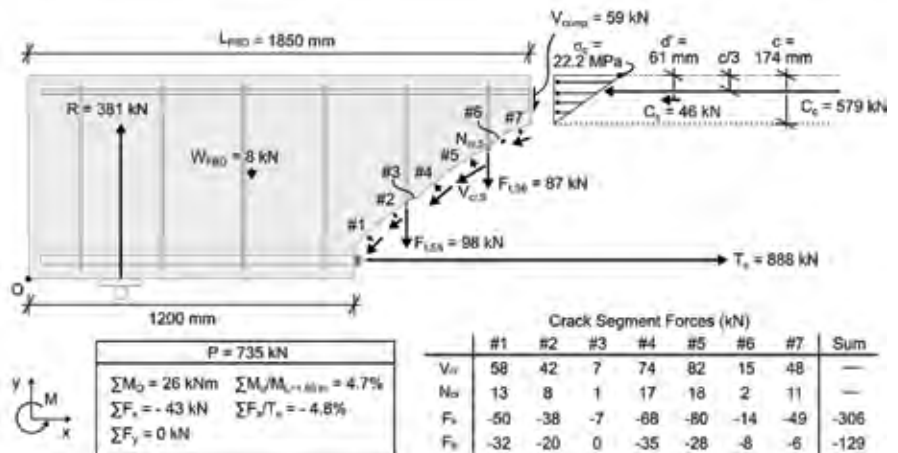
**Fig. 5: Free body diagram (FBD) of beam JP-2 at P = 735 kN, where force components are calculated from DFOS strain and DIC crack width and slip measurements**

Fig. 2 and multiplied by the reinforcement area.[3] The force in the tension reinforcement was found using the same process for the 35M reinforcing bars at the observed crack location. The compressive concrete force ($C_c$) and compressive reinforcement force ($C_s$) were found by assuming plane sections remain plane at the cut location ($L_{FBD}$), where the compressive strain profile was assumed to be linear and defined using the DFOS strains from the top and bottom reinforcement at that location to determine the neutral axis depth ($c$). To determine $C_c$, the strains were converted to stresses using the elastic modulus from Eurocode 2,[11] which equalled 31.5 GPa, as this was found to model the short-term behavior of the concrete better than the ACI Code equation.[12] Lastly, the normal and shear crack forces ($N_{cr}$ and $V_{cr}$) were found using the measured distributed crack width and slip measurements from the DIC analysis and an aggregate interlock model known as the contact density model.[13] From these measurements, the shear and normal stresses on the crack surface could be estimated, which were then multiplied by the crack area.

Based on the distributed measurements and material models, this approach resulted in an FBD that is close to being in equilibrium, with a 26 kN·m imbalance in the moment and −43 kN imbalance in the x-direction. When these imbalances are compared to the applied moment at the cut face ($M_{L=1.85\,m}$) and the tension steel force ($T_s = 888$ kN), the FBD is only imbalanced by about 5%, which given the potential variation in parameters such as the modulus of elasticity and the stress carried along the crack is very promising. In this analysis, the y-direction is in perfect equilibrium because the remaining vertical force was set to equal the unknown shear force in the flexural compression region ($V_{comp}$). At $P = 735$ kN, $V_{comp}$ represented 15% of the reaction force ($R$) which is close to the ~20% value that Mörsch[14] predicted over 100 years ago.

The FBD being close to equilibrium without modifications to the constitutive models implies a number of conclusions: 1) there is shear carried in the flexural compression region of members with stirrups, but it is a relatively small contribution; 2) it is realistic to assume, for slender members like these with stirrups, that the concrete contribution ($V_c$) is the integral of aggregate interlock stresses along the crack plus the small compression region force; and 3) the source of the stirrup contribution to shear strength ($V_s$) is the force in stirrups crossing the cracks. Note that the pair of fiber optic cables on each bar allowed bar bending and dowel action in stirrups and flexural reinforcement to be evaluated. These forces were found to be small[10] and thus are not shown in Fig. 5.

In addition to the core conclusions previously mentioned, another observation from the FBD in Fig. 5 comes from the magnitude of the flexural compression and tensile forces. It is apparent that the tension force arrow ($T_s = 888$ kN) and combined compression force arrows ($C_c + C_s = 625$ kN) are unequal. Indeed, the difference of 263 kN is 10 times the self-weight of the beam and thus much more than a measurement error. The reason this occurs is that the aggregate interlock forces on the crack provide a vertical component carrying shear but also a significant horizontal component.

Lest the reader was to conclude that the shear on the crack is not the primary source of $V_c$, consider that if normal and shear crack forces ($N_{cr}$ and $V_{cr}$) were ignored, the x-imbalance would climb to the noted 263 kN, with a similar increase to the moment imbalance. In the vertical direction, the lack of aggregate interlock would also cause the calculated shear in the compression region to equal 49% of the reaction force or an equivalent maximum shear stress of 5.43 MPa. This shear stress combined with the axial stress in Fig. 5 would exceed the diagonal cracking strength in the compression chord, yet this cracking was not observed in the test. Therefore, the assumption that all the $V_c$ shear is carried in the compression region cannot be the full story.

## Effect of shear on longitudinal behavior

One cause of the difference in the tension and compression forces in the FBD of Fig. 5 is because these regions are not just resisting flexure but also shear. This mechanism is highlighted in the DFOS strain measurements of the top and bottom reinforcements in a combined distributed measurement (CDM) plot in Fig. 6.[8] This figure shows the DFOS strains spaced every 10 mm along the longitudinal reinforcement bars from JP-2 at an applied point load of 735 kN. The measured tensile (shaded in blue) and compressive (shaded in green) DFOS
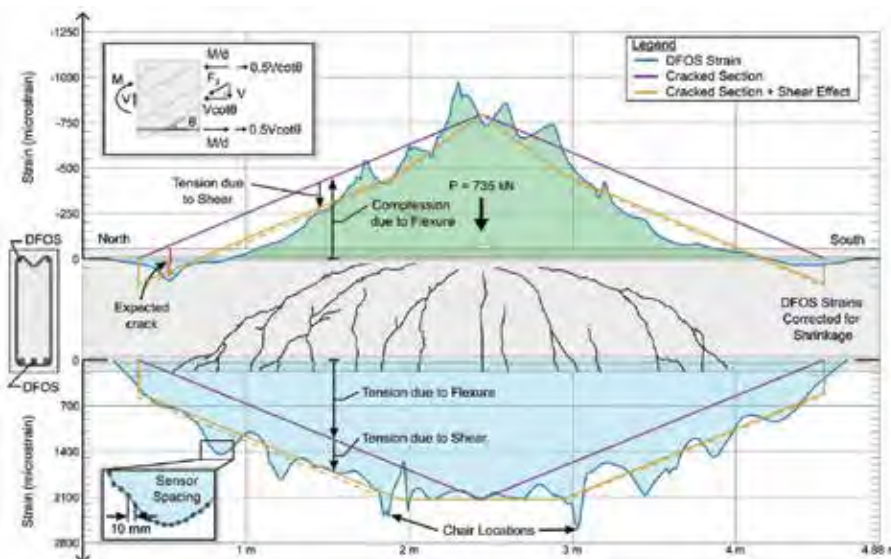


**Fig. 6: Combined distributed measurement (CDM) plot of specimen JP-2 at *P* = 735 kN with compressive and tensile reinforcement strains**

strains are compared to predictions based on several cracked section analyses (the purple and gold lines). The CDM is plotted with the corresponding cracking pattern, which contains diagonal shear cracking on both shear spans. The DFOS strains from the tensile reinforcement are not linear with beam length due to tension stiffening effects along the bar. However, the measured DFOS strains also do not follow the transformed cracked section estimate, drawn in purple and labeled as Cracked Section. Generally, the tension reinforcement DFOS strains were significantly higher than the Cracked Section strains, while the compressive reinforcement strains were significantly lower than the Cracked Section strains, particularly away from midspan.

This effect, sometimes called a moment shift, can be explained by the inset FBD in Fig. 6. If the member is assumed to be diagonally cracked with a series of parallel cracks, a field of diagonal compression will form in the web of the member to carry the shear, which also results in an additional horizontal force of $V\cot\theta$. This horizontal compressive component is centered in the web and thus can be modeled as resisted by two additional horizontal tensile forces of $0.5V\cot\theta$, one at the level of the tension reinforcement and the other within the flexural compression region. The Cracked Section + Shear Effect prediction with the gold line fits the measured DFOS strain data more closely than a flexure-only approach. Thus, the argument that the difference in horizontal flexural forces on the top and bottom of the section are caused by aggregate interlock stresses is only part of the story: locally at the crack they are caused by aggregate interlock, but on average they can also be derived directly from the shear stresses themselves assuming only that the member is diagonally cracked. This sort of triangulation of evidence suggests that the analysis in this article is on the right track.

A critical parameter in the Cracked Section + Shear Effect prediction is the angle of principal compressive stress ($\theta$). In the case of the Cracked Section + Shear Effect prediction in Fig. 6, $\theta$ was taken as 45 degrees, which ACI 318 recommends for shear design.[15] An alternative approach is to determine the average angle of diagonal principal compressive stress experimentally through fitting the Cracked Section + Shear Effect prediction to the DFOS tension reinforcement strain.[10,12] This approach was applied to the data in Fig. 6, as indicated by the dashed gold line. At $P$ = 735 kN in Fig. 6, $\theta$ was found to be 28 degrees on the north span and 31 degrees on the south span. This hints at a potential opportunity to refine Code approaches and will be discussed further.

Another consequence of the shear cracking is that the $0.5V\cot\theta$ component on the compressive side reduces the measured strain to such an extent that tension is both measured and predicted in the top chord of the beam, where the bending moment is small near the support. This behavior can be seen in Fig. 6, where over the north support, a location exists where the compressive reinforcement strain exceeds the cracking strain of the concrete and, thus, a crack was likely present, though it was too small for the authors to locate. This leads to an interesting consideration for design, in that reinforcement is required in an area where one might typically assume it is not needed for flexure alone.

## Stirrup response

Another key to unlocking the riddle of shear is to understand the response of the transverse reinforcement so that the ACI 318 $V_s$ term can be evaluated. DFOS strain results from one of the stirrup legs of stirrup S6 in beam JP-2 are displayed in Fig. 7(b). Stirrup S6 was located 1.69 m from the north end and crossed several shear cracks (Fig. 7(a)), as reflected in the peaks in strain observed over the height of the stirrup. It is clear from these DFOS results that the response of a stirrup is highly variable over the member height. Therefore, a single strain gauge is inadequate for measuring the stirrup demand because it cannot be guaranteed that the gauge will be at the crack location and hence measure the critical strain.

Meanwhile, the stresses in the stirrup are shown in Fig. 7(c). The distributed stress profile for the stirrup was more constant over the height versus the strain response, particularly at the highest applied load levels (735 kN and 828 kN) and where the shear cracks crossed near the top of the member. This is in line with the ACI 318 Code provisions for stirrup forces at ULS conditions where it is assumed the stirrups will yield. It is also apparent from Fig. 7(c) that the demand near the top
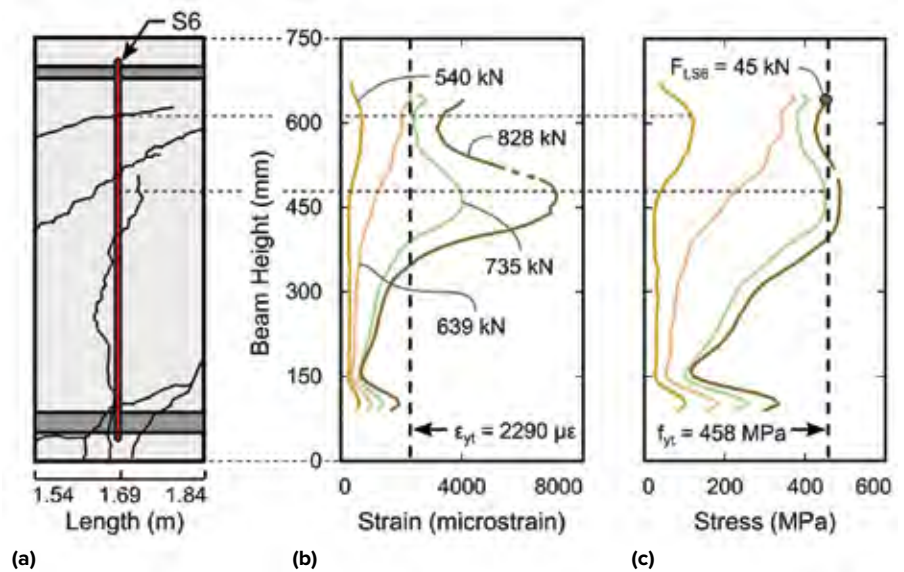


Fig. 7: Demand of stirrup JP-2 S6: (a) cracking pattern at JP-2 S6 location; (b) DFOS strains; and (c) reinforcement stresses
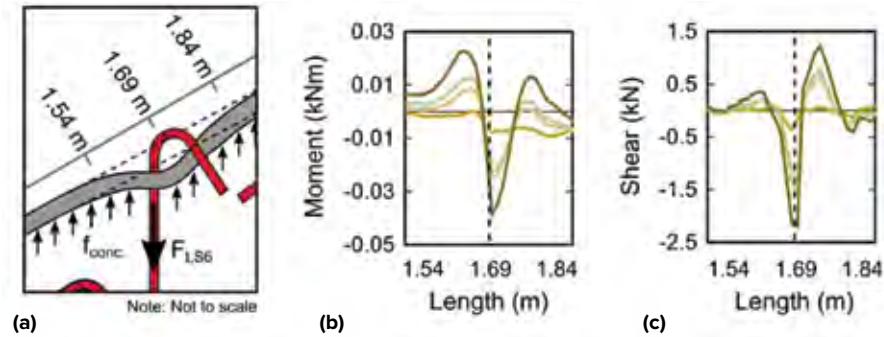
**Fig. 8: Impact of high hook forces: (a) schematic of anchorage-induced compression bar bending; (b) measured moment of 20M compressive reinforcement; and (c) measured shear of 20M compressive reinforcement**
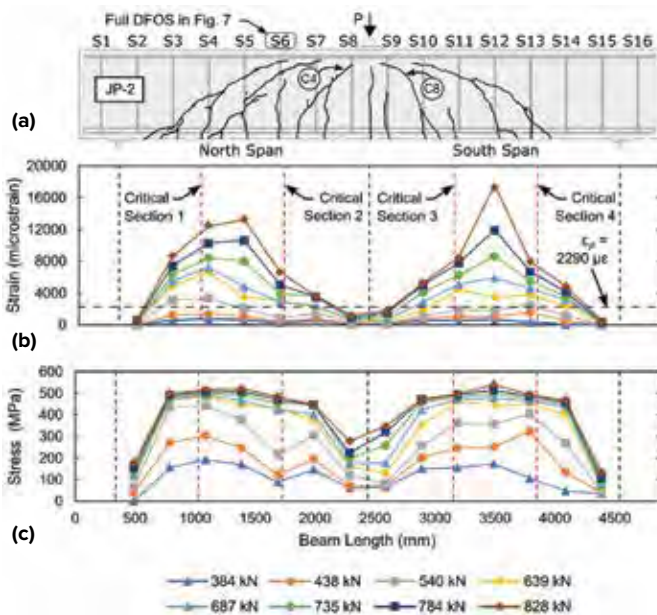


**Fig. 9: Peak stirrup demand for all stirrups in JP-2: (a) cracking pattern for JP-2 at ULS; (b) strains from DFOS; and (c) stresses**

hook of the stirrup was high, equaling 45 kN (98% of yield) at ULS. This meant the demand on the 135-degree stirrup hook was high even though the hook was on the flexural compression side of the member but also in flexurally uncracked concrete. This observation was found for many stirrup leg measurements from JP-1, JP-2, and JP-3, where diagonal shear cracks crossed near the top of the stirrup leg, highlighting the importance of proper stirrup detailing even in the uncracked flexural compression region.

The impact of these high hook forces can also be seen in the flexural compression reinforcement strains, where the stirrup anchorage force induced bending as depicted in Fig. 8(a).[5,8] Because the observed bending in Fig. 8(b) must have an associated shear force diagram, the approximate amount of shear transmitted by the stirrup hook to the compressive reinforcement can be found as presented in Fig. 8(c) (total shear force measured from peak to trough). While

the ~4 kN shear force at ULS is small relative to the 45 kN tension force measured at the top of the east stirrup leg in Fig. 7(c), this demonstrates the potential that distributed sensors offer in terms of understanding and indeed quantifying complex shear behavior.

While Fig. 7 shows the DFOS measurements of a single stirrup leg, Fig. 9 summarizes the peak demand of all the stirrups in specimen JP-2 for loads after shear cracking. The measured peak strains averaged between the two stirrup legs are presented for the 14 stirrups in Fig. 9(b) while the corresponding stresses are plotted in Fig. 9(c). Figure 9(b) shows how increasing the applied load resulted in increased stirrup strains generally, where the maximum was found in the critical region for shear design (*d* from the supports and point load as in ACI 318). The highest measured strain was in S12 at the ULS load stage (*P* = 828 kN or 96% of the peak load), where the strain exceeded 16,000 microstrain or 1.6% strain in the shear span where the shear failure was observed. The lowest stirrup strains were measured where the shear force diagram approached zero or switched signs in the S2 and S15 stirrups near the support plates and the S8 and S9 stirrups near the load plate.

The peak stirrup stresses, however, tell a different story where the stirrup stress demand was essentially constant along the entire shear span. This occurred because the stirrups were almost all yielding for most of the load levels as shown in Fig. 9(b) and (c), except near the disturbed regions at the member ends. Importantly, the stirrups were observed to yield as early as *P* = 540 kN (62% of the peak load), clearly demonstrating that reinforced concrete members do not fail once a stirrup first yields—a common misconception. Additional applied load can be resisted due to the rotating angle of the principal compressive stress field, when considered in an average sense, or with additional shear on the crack, when considered locally at the crack.

Another finding from Fig. 9(c) is how high the peak stresses increased for the stirrups nearest to the point load (S8 and S9), which is a region where lower demand in the stirrups might be expected since they were within a distance (*d*) of the load plate. However, because cracks C4 and C8 turn towards the point load, the cracks intercept S8 and S9, causing nearly 400 MPa of stress at ULS conditions. Meanwhile, clamping action prevents cracks from forming near the pin and roller supports, explaining why the measured strains and stresses are relatively lower for S2 and S15.

## Shear resistance reinforcement and concrete contribution

Using the distributed measurements over the height of the stirrups, the resistance which stirrups provide along a crack

($V_s$) can be quantified. The experimentally determined $V_s$ for eight shear cracks in beams JP-1, JP-2, and JP-3 are presented in Fig. 10. The curves represent the cumulative stirrup forces which cross the shear cracks determined from the DFOS strain measurements. For example, for crack JP-3 C1, the $V_s$ curve is made up of a total of four stirrups, where $V_s$ is the total stirrup force from stirrups S5 to S8. As expected, the $V_s$ was approximately zero for the three beams before shear cracking. But once shear cracking occurred, the $V_s$ for most cracks does not equal the reaction force (they are below the 1:1 line in the figure). Therefore, some other mechanism must contribute to resisting shear even at low applied loads, namely the concrete contribution $V_c$. However, in the case of crack JP-2 C1, the $V_s$ exceeds the applied shear for some load levels. This is attributed to the flatter portion of crack JP-2 C1 requiring high enough normal compressive stresses on the crack interface to allow $V_s$ to exceed the reaction force. In Fig. 5, these normal stresses are labeled $N_{cr}$ and can be seen

to be predicted to be comparatively low for that crack geometry.

The behavioral differences in the shear crack $V_s$ curves between the three beams show interesting trends worthy of a closer look. Generally, the shear resisted by $V_s$ for JP-1 and JP-2 begin to plateau as the loading approaches ULS, while JP-3 has a more linear response up to ULS. This was because the stirrups of JP-1 and JP-2 were yielding, as shown in Fig. 7 and 9 for JP-2, and thus the value of $V_s$ was limited while for JP-3, the member reached flexural yield prior to a shear failure, limiting the demand on $V_s$. Figure 10 shows that immediately after diagonal cracking, the concrete and stirrup components ($V_c$ and $V_s$) both contribute to the shear resistance. Given that the $V_s$ curves are approximately parallel to the 1:1 applied load line, the amount of $V_c$ was reasonably constant during loading until the stirrups started to yield. At this point, the $V_s$ term could not increase; thus, any additional shear must have been resisted by $V_c$ alone. Eventually, this mechanism would also reach a limit as higher loads are associated with wider cracks and lower aggregate interlock capacity, so eventually the cracks would begin to slip uncontrollably—a shear failure.

The experimentally measured $V_s$ values at ULS conditions from Fig. 10 are compared to the predictions of shear resistance ($V_n = V_s + V_c$) from ACI 318 in Fig. 11. For this study, all safety factors equalled unity. For the three shear reinforcement ratios tested, ACI 318 provided reasonable but fairly conservative estimates for $V_s$. Other design methods, such as the CSA[16] or "AASHTO LRFD Bridge Design Specifications,"[17] assume lower values of θ and thus predict a higher value of $V_s$ closer to the average behavior shown in
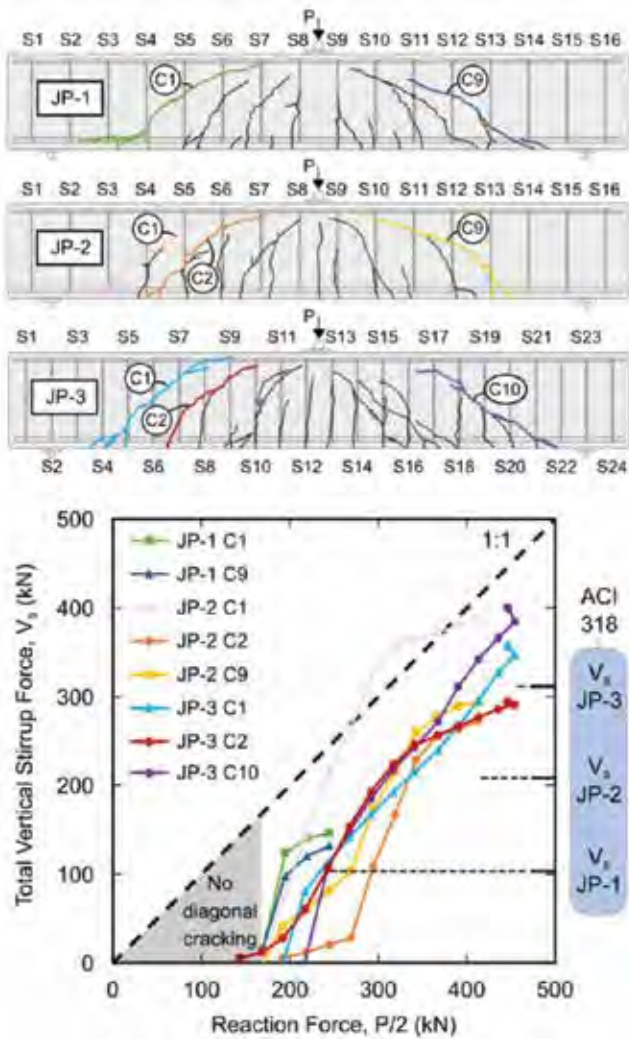


Fig. 10: Measured $V_s$ with load calculated using DFOS strains for eight shear cracks from JP-1, JP-2, and JP-3, compared to ACI 318 Code predictions
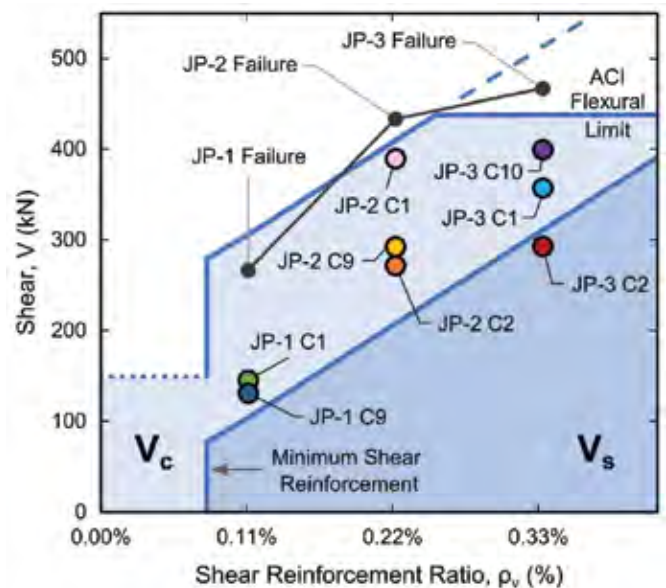


Fig. 11: Measured $V_s$ of JP-1, JP-2, and JP-3 cracks at ULS conditions compared to $V_s + V_c$ estimate from ACI 318, and failure load of three beams

Fig. 11.[10] Figure 11 shows via the black line that the ACI Code made good predictions of the failure load, where the code-to-experimental failure load ratio was between 0.94 and 1.14. The other codes, CSA and AASHTO, produced similar predictions of failure load where the code-to-experimental failure load ratio was between 0.90 and 1.11. While each method provided similarly good $V_s + V_c$ predictions, the ACI Code has a lower $V_s$ term, meaning that it must also have a higher $V_c$ value than the other codes in order to produce a similar sum. The recent drop of the $V_c$ value of members without stirrups in ACI 318-19 due to the size effect could be related to this difference as well, though more study is required to know if this is true in general.

## Summary and Key Findings

This study demonstrated how distributed sensing is a useful tool for unraveling the riddle of shear. The results were used to evaluate reinforced concrete behavior in comparison to the ACI 318 Code provisions and further the understanding of how shear is carried. The key findings from this study include:

- Shear deflections can represent about 25% of the total deflection at service conditions for transfer girders, and up to 42% at ULS for members meeting minimum shear reinforcement requirements from ACI 318;
- Distributed measurements enable the individual shear force carrying mechanisms to be quantified and understood, namely $V_s$, $V_c$, and shear in the compression region ($V_{comp}$). It was shown that considering aggregate interlock was necessary to maintain equilibrium;
- Cracked reinforced concrete flexural members experience increased horizontal tension demand in the reinforcement due to shear and lower compression demands on the compression face. These decreased compression demands can cause cracks to form on the flexural compression face near regions of high shear and low moment demand (for example, at the support in simply supported members);
- Member failure does not typically occur at the onset of stirrup yielding as the rotating angle of the principal compressive stress field allows for higher shear to be resisted by making the principal compression stress in the concrete that carries the shear more efficient; and
- For the measured $V_s$ at ULS conditions, ACI 318 was

shown to conservatively estimate $V_s$ while the failure loads were estimated within 14% of the experimental values.

## References

1. Belarbi, A.; Kuchma, D.A.; and Sanders, D.H., "Proposals for New One-Way Shear Equations for the 318 Building Code," *Concrete International*, V. 39, No. 9, Sept. 2017, pp. 29-32.

2. Kani, G.N.J., "The Riddle of Shear Failure and its Solution," *ACI Journal Proceedings*, V. 61, No. 4, 1964, pp. 441-468.

3. Collins, M.P., and Mitchell, D., *Prestressed Concrete Structures*, Response Publications, Toronto, ON, Canada, 1991, 393 pp.

4. Kreger, S.T.; Gifford, D.K.; Froggatt, M.E.; Sang, A.K.; Duncan, R.G.; Wolfe, M.S.; and Soller, B.J., "High-Resolution Extended Distance Distributed Fiber-Optic Sensing Using Rayleigh Backscatter," *Proceedings of SPIE*, K.J. Peters, ed., V. 6530, Mar. 29, 2007, 10 pp.

5. Poldon, J.J.; Hoult, N.A.; and Bentz, E.C., "Understanding Reinforcement Behavior Using Distributed Measurements of Shear Tests," *ACI Structural Journal*, V. 118, No. 3, May 2021, pp. 255-266.

6. Stanier, S.A.; Blaber, J.; Take, W.A.; and White, D.J., "Improved Image-Based Deformation Measurement for Geotechnical Applications," *Canadian Geotechnical Journal*, V. 53, No. 5, Oct. 2016, pp. 727-739.

7. Hoult, N.A.; Dutton, M.; Hoag, A.; and Take, W.A., "Measuring Crack Movement in Reinforced Concrete Using Digital Image Correlation: Overview and Application to Shear Slip Measurements," *Proceedings of the IEEE*, V. 104, No. 8, 2016, pp. 1561-1574.

8. Poldon, J.J.; Hoult, N.A.; and Bentz, E.C., "Distributed Sensing in Large Reinforced Concrete Shear Test," *ACI Structural Journal*, V. 116, No. 5, Sept. 2019, pp. 235-245.

9. Sherwood, E.G., "One-Way Shear Behaviour of Large, Lightly-Reinforced Concrete Beams and Slabs," PhD thesis, Department of Civil Engineering, University of Toronto, Toronto, ON, Canada, 2006, 598 pp.

10. Poldon, J.J.; Hoult, N.A.; and Bentz, E.C., "Understanding Shear-Resistance Mechanisms in Concrete Beams Monitored with Distributed Sensors," *ACI Structural Journal*, V. 119, No. 6, Nov. 2022, pp. 329-340.

11. EN 1992-1-1, "Eurocode 2: Design of Concrete Structures - Part 1-1: General Rules and Rules for Buildings," European Committee for Standardization, Brussels, Belgium, Dec. 2004, 227 pp.

12. Poldon, J.J.; Bentz, E.C.; and Hoult, N.A., "Assessing Beam Shear Behavior with Distributed Longitudinal Strains," *Structural Concrete*, V. 23, No. 3, June 2022, pp. 1555-1571.

13. Maekawa, K.; Pimanmas, A.; and Okamura, H., *Nonlinear Mechanics of Reinforced Concrete*, CRC Press, Boca Raton, FL, 2019, 721 pp.

14. Mörsch, E., "Der Eisenbetonbau: seine Theorie und Anwendung," Konrad Wittwer, Stuttgart, Germany, 1908, 376 pp. (in German)

15. ACI Committee 318, "Building Code Requirements for Structural Concrete (ACI 318-19) and Commentary (ACI 318R-19)," American Concrete Institute, Farmington Hills, MI, 2019, 623 pp.

16. CSA Committee A23.3, "Design of Concrete Structures," Canadian Standards Association, Rexdale, ON, Canada, 2019, 301 pp.

17. "AASHTO LRFD Bridge Design Specifications," ninth edition, American Association of State Highway and Transportation Officials, Washington, DC, 2020, 1912 pp.

Selected for reader interest by the editors.

**Jack J. Poldon** is an Engineer-in-Training at RJC Engineers in Toronto, ON, Canada. His consulting work involves the structural design of healthcare, institutional, and sport facilities. He received his BASc in 2017 and PhD in 2022, both from Queen's University, Kingston, ON, Canada.

**Neil A. Hoult** is a Professor in the Department of Civil Engineering at Queen's University. His research interests include the behavior of reinforced concrete structures and monitoring technologies for the assessment of infrastructure. He received his BASc and MASc from the University of Toronto, ON, Canada, and his PhD from the University of Cambridge, Cambridge, UK.

**Evan C. Bentz**, FACI, is Professor and Associate Chair (undergrad) of civil engineering at the University of Toronto. He is a member and past Chair of ACI Committee 365, Service Life Prediction, and a member of Joint ACI-ASCE Committee 445, Shear and Torsion. He received the 2018 ACI Chester Paul Seiss Award and the 2006 and 2017 ACI Design Award. He received his BASc from the University of Waterloo, Waterloo, ON, Canada, in 1994 and his PhD from the University of Toronto in 2000.